



X-ray spectral and timing evolution of MAXI J1727–203 with *NICER*

K. Alabarta^{1,2,★}, D. Altamirano,¹ M. Méndez,² V. A. Cúneo^{3,4}, L. Zhang^{5,1}, R. Remillard,⁵
A. Castro^{6,1,6}, R. M. Ludlam,⁷ J. F. Steiner,⁸ T. Enoto,^{9,10} J. Homan,^{11,12} Z. Arzoumanian,¹³ P. Bult,^{13,14}
K. C. Gendreau,¹³ C. Markwardt,¹³ T. E. Strohmayer,¹³ P. Uttley,¹⁵ F. Tombesi^{13,14,16} and D. J. K. Buisson¹

¹School of Physics and Astronomy, University of Southampton, Southampton SO17 1BJ, UK

²Kapteyn Astronomical Institute, University of Groningen, PO Box 800, NL-9700 AV Groningen, the Netherlands

³Instituto de Astrofísica de Canarias (IAC), Universidad de La Laguna, Vía Láctea s/n, La Laguna E-38205, S/C de Tenerife, Spain

⁴Departamento de Astrofísica, Universidad de La Laguna, La Laguna, E-38205, S/C de Tenerife, Spain

⁵MIT Kavli Institute for Astrophysics and Space Research, MIT, 70 Vassar Street, Cambridge, MA 02139, USA

⁶Consortio de Investigación del Golfo de México, CICESE, Carretera Ensenada-Tijuana 3918, 22860 Ensenada, BC, Mexico

⁷Cahill Center for Astronomy and Astrophysics, California Institute of Technology, Pasadena, CA 91125, USA

⁸Center for Astrophysics, Harvard & Smithsonian, 60 Garden Street, Cambridge, MA 02138, USA

⁹Extreme Natural Phenomena RIKEN Hakubi Research Team, RIKEN Cluster for Pioneering Research, 2-1 Hirosawa, Wako, Saitama 351-0198, Japan

¹⁰The Hakubi Center for Advanced Research, Kyoto University, Kyoto 606-8302, Japan

¹¹Eureka Scientific, Inc., 2452 Delmer Street, Oakland, CA 94602, USA

¹²SRON, Netherlands Institute for Space Research, Sorbonnelaan 2, NL-3584 CA Utrecht, the Netherlands

¹³Astrophysics Science Division, NASA Goddard Space Flight Center, Greenbelt, MD 20771, USA

¹⁴Department of Astronomy, University of Maryland, College Park, MD 20742, USA

¹⁵Anton Pannekoek Institute for Astronomy, University of Amsterdam, Science Park 904, NL-1098 XH Amsterdam, the Netherlands

¹⁶Department of Physics, University of Rome ‘Tor Vergata’, Via della Ricerca Scientifica 1, I-00133 Rome, Italy

Accepted 2020 July 20. Received 2020 July 20; in original form 2020 April 8

ABSTRACT

We present a detailed X-ray spectral and variability study of the full 2018 outburst of MAXI J1727–203 using *NICER* observations. The outburst lasted approximately four months. Spectral modelling in the 0.3–10 keV band shows the presence of both a soft thermal and a hard Comptonised component. The analysis of these components shows that MAXI J1727–203 evolved through the soft, intermediate, and hard spectral states during the outburst. We find that the soft (disc) component was detected throughout almost the entire outburst, with temperatures ranging from ~ 0.4 keV, at the moment of maximum luminosity, to ~ 0.1 keV near the end of the outburst. The power spectrum in the hard and intermediate states shows broad-band noise up to 20 Hz, with no evidence of quasi-periodic oscillations. We also study the rms spectra of the broad-band noise at 0.3–10 keV of this source. We find that the fractional rms increases with energy in most of the outburst except during the hard state, where the fractional rms remains approximately constant with energy. We also find that, below 3 keV, the fractional rms follows the same trend generally observed at energies > 3 keV, a behaviour known from previous studies of black holes and neutron stars. The spectral and timing evolution of MAXI J1727–203, as parametrised by the hardness–intensity, hardness–rms, and rms–intensity diagrams, suggest that the system hosts a black hole, although we could not rule out a neutron star.

Key words: Accretion, accretion discs – black hole physics – X-rays: binaries – X-rays: individual: MAXI J1727–203.

1 INTRODUCTION

Low-mass X-ray binary (LMXB) systems are binaries that contain a compact object, either a black hole (BH) or a neutron star (NS) and an evolved low-mass companion star. LMXB systems for which the compact object is a BH candidate are known as BH LMXBs. The energy spectra of BH LMXBs are characterised by two main components: a soft thermal component and a hard power law like component (e.g. Remillard & McClintock 2006; Belloni 2010). The thermal component is generally described by a multicolour disc blackbody model (Mitsuda et al. 1984) peaking at 1–2 keV (see review by Done, Gierliński & Kubota 2007 and references

therein) and thought to be produced by a geometrically thin and optically thick accretion disc (Shakura & Sunyaev 1973). The hard component is thought to be produced by a region of hot plasma, around the compact object and the accretion disc (the so-called ‘corona’; Sunyaev & Truemper 1979; Sunyaev & Titarchuk 1980). A thermal Comptonisation model, in which high-energy photons are emitted by inverse Compton scattering (Sunyaev & Titarchuk 1980), has been proposed to explain the hard component of the BH LMXBs energy spectra (e.g. Titarchuk 1994; Zdziarski & Gierliński 2004; Done et al. 2007; Burke, Gilfanov & Sunyaev 2017).

BH LMXBs show a variety of spectral and timing properties during an outburst (see e.g. van der Klis 1989, 2000; Méndez & van der Klis 1997; Homan & Belloni 2005; Remillard & McClintock 2006; Belloni 2010; Belloni, Motta & Muñoz-Darias 2011; Plant et al.

* E-mail: k.alabarta@soton.ac.uk

2014; Motta 2016). Two main spectral states can be defined (see e.g. Tanaka 1989; van der Klis 1994): the low/hard state (LHS), when the thermal Comptonised component dominates the energy spectrum and the high/soft state (HSS), when the thermal component dominates the spectrum. In the LHS, however, a multicolour disc blackbody component can be detected (e.g. Capitanio et al. 2009; Wang-Ji et al. 2018). In this state, the power-density spectrum (PDS) is characterised by a strong broad-band noise component with a fractional rms amplitude of 30–50 per cent (e.g. Méndez & van der Klis 1997; Belloni et al. 2005; Remillard & McClintock 2006; Muñoz-Darias, Motta & Belloni 2011; Motta 2016). In addition, quasi-periodic oscillations (QPOs) of type-C can be detected (e.g. Casella et al. 2004; Belloni et al. 2005). These oscillations have a centroid frequency ranging from 0.01 to 30 Hz. In the HSS, a weak power-law component is sometimes detected in the energy spectrum (e.g. Capitanio et al. 2009). The broad-band fractional rms of BHs in this state is generally less than 5 per cent (Méndez & van der Klis 1997) and QPOs are sometimes detected too (e.g. Remillard & McClintock 2006; Muñoz-Darias et al. 2011; Motta 2016).

Between the LHS and HSS, two intermediate states can be distinguished in terms of variability: the hard intermediate state (HIMS) and the soft intermediate state (SIMS) (see, e.g. Homan & Belloni 2005; Belloni 2010). The HIMS shows less broad-band fractional rms than the hard state (10–30 per cent; e.g. Muñoz-Darias et al. 2011; Motta et al. 2012) and type-C QPOs can be present (e.g. Casella et al. 2004; Belloni et al. 2005; Belloni & Stella 2014). The SIMS is characterised by a weak power-law noise component that replaces the broad-band noise component present in the HIMS and type-A or type-B QPOs (e.g. Wijnands, Homan & van der Klis 1999; Homan et al. 2001; Casella et al. 2004; Belloni et al. 2005; Belloni & Stella 2014). Type-B QPOs have centroid frequencies in the 1–7 Hz frequency range (Gao et al. 2017) and a quality factor, $Q > 6$. Type-A QPOs have centroid frequencies in the 6.5–8 Hz frequency range and are broader than type-B and type-C QPOs, with a quality factor of $Q = 1$ –3 (Wijnands et al. 1999; Casella et al. 2004; Belloni & Stella 2014).

The evolution of a BH LMXB through an outburst can be well illustrated using the hardness–intensity diagram (HID; e.g. Homan et al. 2001; Belloni et al. 2006; Remillard & McClintock 2006). At the beginning of the outburst, the source is in the LHS and its intensity increases at approximately constant hardness ratio, drawing a vertical line in the right part of the HID. At some point in the outburst evolution, the source starts a transition to the HSS, moving to the left in the diagram at an approximately constant luminosity. This transition corresponds to the top horizontal branch in the HID (HIMS and SIMS), reaching the HSS at the top left-hand part of the HID. During the HSS, the source starts to decrease its intensity, moving down in the diagram. Eventually, the source returns to the HIMS and SIMS, drawing a horizontal branch in the HID, but in the opposite direction, from left- to right-hand side. Before the end of the outburst, the source reaches the hard state again to finally return to quiescence. This very particular pattern in the HID of BH LMXBs is known as the q-track and it is often discussed in terms of hysteresis (e.g. Miyamoto et al. 1995). Multiple outbursts of different sources follow this q-track: e.g. XTE 1550–564, GX 339–4, H1743–322, and GRO J1655–40 (Homan et al. 2001; Belloni et al. 2005; Fender, Homan & Belloni 2009; Dunn et al. 2010; Uttley & Klein-Wolt 2015).

The outburst evolution can also be analysed using the hardness–rms diagram (HRD, Belloni et al. 2005) and the rms–intensity diagram (RID, Muñoz-Darias et al. 2011). The different spectral states show different fractional rms-hardness ratio correlations.

Observations in the LHS are located on the top right-hand side of the HRD. When the source enters the HIMS and the SIMS, it moves to the bottom left-hand side of the HRD diagonally until the source reaches the HSS. Finally, the evolution reverses, returning to the HIMS and the SIMS following the same track as before, until it reaches the hard state again at the top right-hand side of the HRD. The evolution in the RID is counterclockwise, similar to the one observed in the HID. In the LHS, the source evolves along a diagonal line from the bottom left-hand to the top right-hand side of the diagram. This line is called the ‘Hard Line’ (HL, Muñoz-Darias et al. 2011). When it makes the transition to the HIMS and SIMS, the source moves horizontally to the left-hand side of the RID. Then, the source reaches the HSS and starts to move down along a diagonal line following the 1 per cent rms line. Finally, the source returns to the HIMS and SIMS moving horizontally to the right-hand side of the diagram. At some point, the source reaches again the 30 per cent rms line and goes down diagonally following the so-called ‘Adjacent Hard Line’ (AHL), which is coincident to the Hard Line.

LMXB systems in which the compact object is an NS are known as NS LMXBs. The energy spectra of NS LMXBs are characterised by three components: a disc blackbody component and a Comptonised component as for BH LMXBs, and a blackbody component from the emission of the surface of the NS and its boundary layer (e.g. Mitsuda et al. 1984; Di Salvo et al. 2000; Gierliński & Done 2002; Lin, Remillard & Homan 2007). NS LMXBs show different X-ray spectral states (for a review, see van der Klis 2006). At high accretion rates, NS LMXBs follow Z-tracks in the HID and the colour–colour diagrams. These sources are known as Z sources. At low accretion rates, NS LMXBs are known as atoll sources due to the tracks they follow in colour–colour diagrams (Hasinger & van der Klis 1989). Atoll sources show three X-ray spectral states that are comparable to the X-ray spectral states of BH LMXBs (e.g. van der Klis 2006; Muñoz-Darias et al. 2014). Besides, the hysteresis observed in BH LMXBs has also been observed in NS LMXBs (Muñoz-Darias et al. 2014), sometimes even the q-track (Körding et al. 2008).

Some differences between BH and NS LMXBs have been observed in the X-ray spectral and timing properties. The hard state of NS systems is softer than that of BH systems (e.g. Done & Gierliński 2003). In terms of timing properties, the most important difference between the two types of LMXBs is the presence of kilo-hertz QPOs (kHz QPOs) at frequencies between 300 Hz and 1.2 kHz for NS (van der Klis 2006; van Doesburgh, van der Klis & Morsink 2018). In terms of the broad-band noise component and low-frequency QPOs (LFQPOs), NSs and BHs systems can be very similar (e.g. Klein-Wolt & van der Klis 2008), but while BH LMXBs usually show broad-band noise up to 500 Hz, NS systems can show broad-band noise at higher frequencies (Sunyaev & Revnivtsev 2000).

MAXI J1727–203 was discovered on 2018 June 5 with MAXI/GSC (Yoneyama et al. 2018). Ludlam et al. (2018b) and Kennea, Bahramian & Beardmore (2018) reported observations performed the same day with the *Neutron star Interior Composition Explorer* (NICER; Gendreau, Arzoumanian & Okajima 2012) and with the Neil Gehrels *Swift* Observatory (*Swift*; Gehrels et al. 2004), respectively. A hard-to-soft state transition and the disc properties of the system in the soft state, led to the possible identification of the source as a BH transient (Negoro et al. 2018). In mid-July of 2018, a soft-to-hard transition was observed with *Swift*/XRT (Tomsick et al. 2018).

NICER (Gendreau et al. 2012) is an X-ray instrument aboard the *International Space Station* (ISS) launched in 2017. It consists of 52 functioning detectors. Photons in the 0.2–12 keV energy band can be detected to a time resolution of 300 ns. In this paper, we present the first study of the spectral and timing evolution of the 4-months long

outburst of MAXI J1727–203 as observed with *NICER*. In Section 2, we describe the observations and data analysis. In Section 3, we present the results of the spectral and timing study. In Section 3.1, we describe the outburst evolution. In Sections 3.2 and 3.3, we describe the timing and spectral properties, respectively. Finally, in Section 4, we discuss the nature of the compact object of the source and the identification of its spectral states.

2 OBSERVATION AND DATA ANALYSIS

NICER observed MAXI J1727–203 86 times between 2018 June 5 and October 7 (ObsID 1200220101–1200220186). The data were analysed using the software HEASOFT version 6.26 and NICERDAS version 6.0. The latest CALDB version 20190516 was used. We applied standard filtering and cleaning criteria, including the data where the pointing offset was <54 arcsec, the dark Earth limb angle was $>15^\circ$, the bright Earth limb angle was $>30^\circ$, and the *ISS* was outside the South Atlantic Anomaly (SAA). We removed data from detectors 14 and 34 which occasionally show episodes of increased electronic noise, so all our results are based on using *NICER*'s 50 other active detectors. Also, we excluded time intervals showing strong background flare-ups, that is, time intervals with an averaged count rate in the 13–15 keV energy band higher than 1 counts s^{-1} . The good time intervals (GTIs) of each observation were separated into several data segments (1–9) based on the orbit of the *ISS*. The background was calculated using the ‘3C 50_RGv5’ model provided by the *NICER* team.

To create the long-term light curve and the HID of the outburst, we first produced 1-s binned light curves in the 0.5–12, 2–3.5, and 6–12 keV energy bands for each data segments using XSELECT. We then applied the background correction for each light curve and calculated averages per data segment. We defined intensity as the average count rate in the 0.5–12 keV energy range and the hardness ratio as the ratio between the 6–12 keV and the 2–3.5 keV band count rates (both background subtracted).

We extracted a background-subtracted energy spectra for each data segment using the ‘3C 50_RGv5’ model mentioned above. We fitted the energy spectra of MAXI J1727–203 in the energy band 0.3–10 keV using XSPEC (V. 12.10.1; Arnaud 1996). We rebinned the spectra by a factor of 3 to correct for energy oversampling and then to have at least 25 counts per bin. In addition, we added a systematic error of 1 percent in the energy range 2–10 keV (suggested by the *NICER* team). We found strong instrumental residuals below 2 keV. These residuals are typical for X-ray missions and Si-based detectors (e.g. Miller et al. 2018; Ludlam et al. 2018a). We therefore added a 5 percent systematic error in the 0.3–2 keV energy band (also suggested by the *NICER* team). We fitted the energy spectra with an absorbed (TBABS in XSPEC; Wilms, Allen & McCray 2000) power-law model, TBABS×POWERLAW, an absorbed disc blackbody (Mitsuda et al. 1984), TBABS×DISKBB, and an absorbed combination of a thermally Comptonisation model (Zdziarski, Johnson & Magdziarz 1996; Życki, Done & Smith 1999) and a multicolour disc blackbody TBABS×(NTHCOMP+DISKBB). Fitting the spectra with the models TBABS×POWERLAW and TBABS×DISKBB did not give satisfactory fits in terms of χ^2/dof and expected spectral parameters. Therefore, in this paper, we only report the results of using the model TBABS×(NTHCOMP+DISKBB). In order to obtain the fluxes of the different components, we added two CFLUX components to the models. The solar abundances were set according to Wilms et al. (2000) and the hydrogen column density (N_H) of the TBABS was left free. The cross-section was set according to Verner et al. (1996). The 1σ errors of

the parameters were calculated from a Markov chain Monte Carlo of length 10 000 with a 2000-step burn-in phase.

For the Fourier timing analysis, we constructed Leahy-normalised power spectra (Leahy et al. 1983) using data segments of 131 seconds and a time resolution of $125 \mu\text{s}$. The minimum frequency was 0.007 Hz and the Nyquist frequency was 4096 Hz. Then, we averaged the power spectra per observation and subtracted the Poisson noise based on the average power in the 3–4 kHz frequency range. Finally, we converted the power spectra to squared fractional rms (van der Klis 1995). We obtained the integrated fractional rms amplitude from 0.01 to 64 Hz. To obtain the rms spectrum (i.e. fractional rms amplitude versus energy), we repeated the previous procedure for the following energy bands: 0.3–0.8, 0.8–2.0, 2.0–5.0, and 5.0–12 keV. We obtained the 0.01–64 Hz fractional rms amplitude for all these bands and plotted the fractional rms amplitude versus energy to study the evolution of the energy dependence of the fractional rms amplitude.

To fit the power spectra, we used a multiLorentzian function: the sum of several Lorentzians. We give the frequency of the Lorentzians in terms of the characteristic frequency, which is the frequency where the component contributes most of its variance per logarithmic interval of frequency (Belloni, Psaltis & van der Klis 2002): $\nu_{\text{max}} = \sqrt{\nu_0 + (\text{FWHM}/2)^2} = \nu_0 \sqrt{1 + 1/4Q^2}$. The quality factor Q is defined as $Q = \nu_0/\text{FWHM}$, where FWHM is the full width at half-maximum and ν_0 the centroid frequency of the Lorentzian.

3 RESULTS

3.1 Outburst evolution

We show the *NICER* light curve of the 2018 outburst of MAXI J1727–203, which covers a period of ~ 123 d, in the 0.5–12 keV energy band in the top panel of Fig. 1. Based on our spectral and variability studies, which are described below, we define four phases of the outburst in Fig. 1: phase A (from MJD 58274 to 58278; shown with orange diamonds), phase B (from MJD 58278 to 58296; shown with blue triangles), phase C (from MJD 58296 to 58322; shown with black circles), and phase D (from MJD 58322 to the end of the outburst; shown with red filled crosses).

The first *NICER* detection of the source was on MJD 58274, at a count rate of $\sim 1400 \text{ counts s}^{-1}$, indicating that the *NICER* observations caught the outburst already at a high flux. The intensity increased very quickly until MJD 58279 in phase A when the source reached a maximum intensity of $\sim 5960 \text{ counts s}^{-1}$. After the maximum, the flux decreased monotonically, although the decay can be divided into 3 parts. As the source entered phase B of the outburst, its intensity decreased smoothly from ~ 5960 to $\sim 3400 \text{ counts s}^{-1}$ over the next 18 d of observation. During phase C of the outburst, the intensity decreased faster than in phase B, from ~ 2500 to $\sim 300 \text{ counts s}^{-1}$ over 26 d. Finally, in phase D the intensity decreased from ~ 90 to $\sim 4 \text{ counts s}^{-1}$ over the last 75 d of X-ray monitoring. After that, the apparent position of the source was located behind the Sun from the point of view of *NICER* in its Earth orbit on-board the *ISS*. After the MAXI J1727–203 occultation by the Sun, *NICER* did not perform further observations of this source.

We also show the 2–10 keV MAXI¹ (Matsuoka et al. 2009) and the 15–50 keV Swift/BAT² (Krimm et al. 2013) light curves of MAXI J1727–203 in the second and third panels of Fig. 1,

¹<http://maxi.riken.jp/pubdata/v6m/J1728-203/index.html>

²<https://swift.gsfc.nasa.gov/results/transients/weak/MAXIJ1727-203.lc.txt>

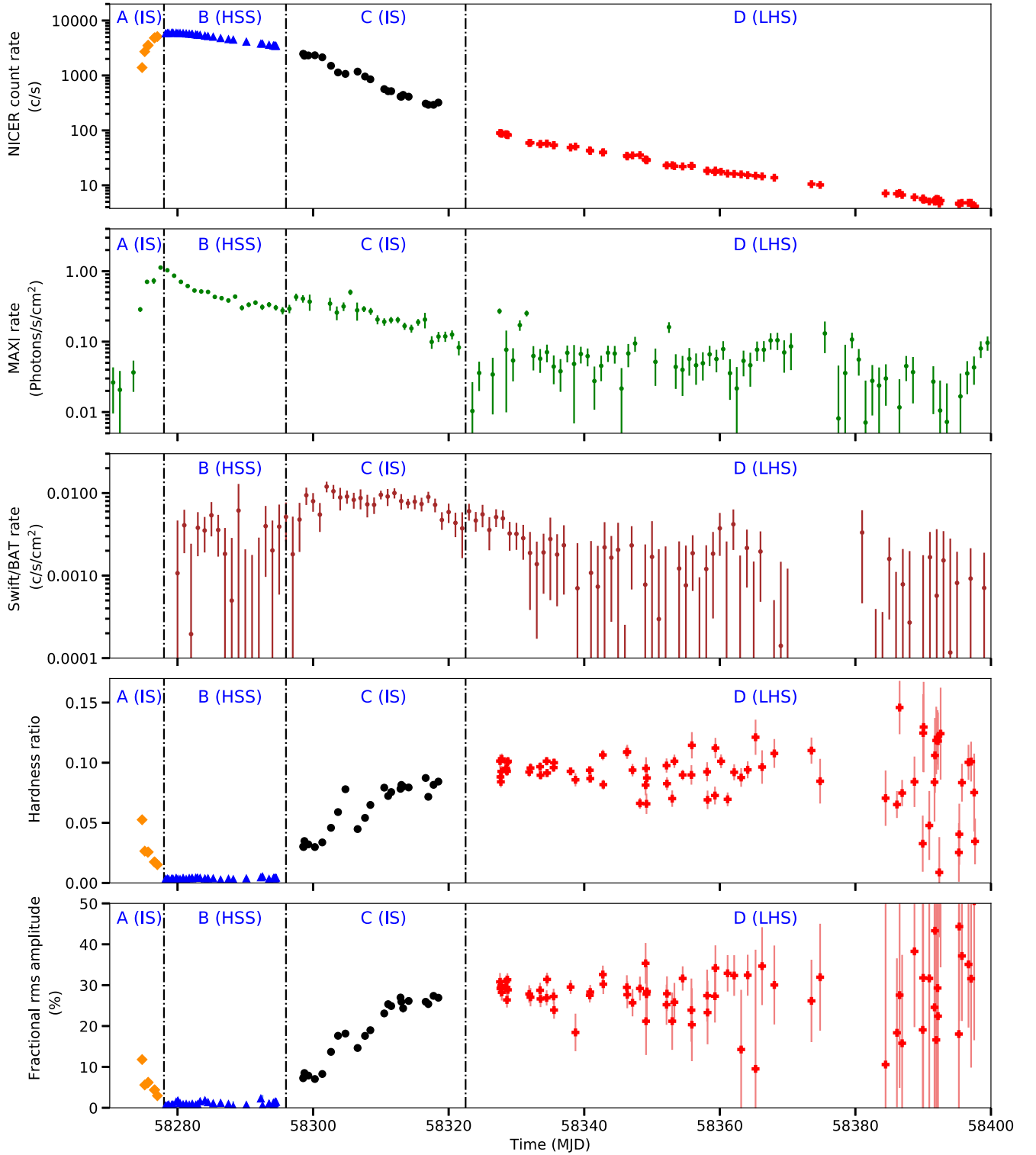


Figure 1. Top panel: *NICER* light curve of the 2018 outburst of MAXI J1727–203 in the 0.5–12 keV energy band. Second panel: *MAXI* light curve of the 2018 outburst of MAXI J1727–203 in the 2–10 keV energy band. Third panel: *Swift*/BAT light curve in the 15–50 keV energy band. Fourth panel: Temporal evolution of the hardness ratio (6–12 keV)/(2–3.5 keV). Bottom panel: Temporal evolution of the 0.01–64 Hz fractional rms amplitude in the 0.5–12 keV energy band. Colours and symbols in the *NICER* light curve, hardness ratio and fractional rms amplitude represent different phases of the outburst. Orange diamonds: phase A, blue triangles: phase B, black circles: phase C, red filled crosses: phase D. The dotted–dashed lines divide the four phases (see Section 4 for a physical interpretation of these intervals).

respectively. The rise of the outburst was detected by *MAXI*, showing that the intensity increased by a factor of ~ 50 in 4 d. In phase B, the *MAXI* intensity decayed faster than the *NICER* intensity. The analysis of the 2–10 keV *NICER* light curve shows the same trend as the 0.5–12 keV light curve, probably indicating that the difference between *NICER* and *MAXI* is due to differences in their respective effective areas. In phases C and D of the outburst, the evolution of both *NICER* and *MAXI* light curves were similar. The *Swift*/BAT light curve did not sample the rise of the outburst, however, it gives additional information during phases B and C, where the 15–50 keV intensity showed a bump. In phases C and D, the *Swift*/BAT intensity decayed until the end of the outburst.

In the fourth panel in Fig. 1, we show the temporal evolution of the hardness ratio (as estimated from *NICER* data) during the whole outburst. The different phases of the outburst show a different behaviour of the hardness ratio. In phase A of the outburst, the hardness ratio drops from ~ 0.05 to ~ 0.02 . In phase B, the hardness ratio remained constant with values around ~ 0.004 . In phase C, the hardness ratio increased from ~ 0.03 to ~ 0.09 . In phase D, the source showed an approximately constant hardness ratio with an average value of ~ 0.09 . Due to the data-gaps between phases B and C, and phases C and D, we arbitrarily chose the limits between phases in the middle of the gap.

In the top panel of Fig. 2, we show the HID. The first point is marked with a green star in the phase A of the outburst (orange diamonds). During this phase, the source evolved in the top part of the HID from the right-hand to the left-hand side. In the phase B of the outburst (blue triangles), the source reduced its intensity at an approximately constant hardness ratio. Then the source entered the phase C of the outburst (black circles) and evolved from the top left-hand to the right-hand side of the diagram. Finally, during the phase D of the outburst (red crosses), the source evolved to the bottom right-hand side of the diagram. Although we are missing the rise of the outburst, a q-track shape is clear in Fig. 2.

3.2 Timing properties

As expected from LMXBs in outburst, the X-ray variability of MAXI J1727–203 also evolved through the 2018 outburst. The bottom panel in Fig. 1 shows the temporal evolution of the averaged fractional rms amplitude. During the first observation (MJD 58274), MAXI J1727–203 showed a fractional rms amplitude of ~ 12 per cent. Then, the fractional rms decreased down to ~ 3 per cent in phase A of the outburst. In phase B, the fractional rms amplitude ranged from ~ 2 to ~ 0.5 per cent, in phase C, it increased from ~ 7 to ~ 27 per cent, and in phase D, it remained approximately constant at ~ 30 per cent.

In the bottom panel of Fig. 2, we show the HRD. The first observation is marked with a green star and it showed a hardness ratio of ~ 0.05 and a fractional rms amplitude of ~ 12 per cent. Then, the source evolved to the bottom left-hand part of the diagram reaching values of the fractional rms amplitude < 1 per cent. Finally, the evolution reversed and the source moved to the top right-hand side of the diagram, increasing its hardness ratio and the fractional rms amplitude.

Fig. 3 shows how MAXI J1727–203 evolves in the absolute rms–intensity diagram. The source described the anticlockwise pattern that has been observed for other BHs (e.g. MAXI J1348–630, Zhang et al., in preparation; GX 339–4, Muñoz-Darias et al. 2011). The first point of the outburst in the RID is denoted with a green star. As the source evolved, it crossed the 10 per cent fractional rms amplitude line increasing its intensity. Two days later, on MJD 58276, the

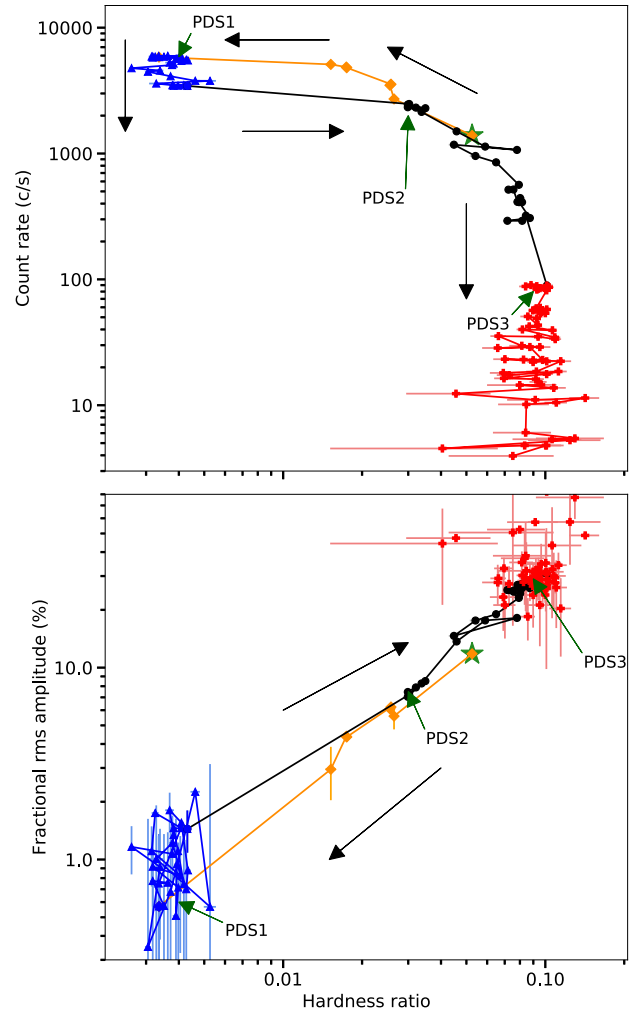


Figure 2. Top panel: HID of MAXI J1727–203 during the 2018 outburst. The hardness ratio is defined as the count ratio in the bands (6–12 keV)/(2.0–3.5 keV). The count rate is obtained in the 0.5–12 keV energy band. Bottom panel: HRD of MAXI J1727–203 during the 2018 outburst. The fractional rms amplitude is obtained in the 0.01–64 Hz frequency range and 0.5–12 keV energy band. The colours are the same as in Fig. 1. The green star marks the first observation. Black arrows indicate the direction of the temporal evolution through the diagram. ‘PDS1’, ‘PDS2’, and ‘PDS3’ mark the location in the plots of the data used to create the representative power spectra shown in Fig. 4. Colours and symbols are the same as described in Fig. 1.

source crossed the 5 per cent line and after that it moved horizontally to the left-hand side of the diagram. From MJD 58278 to 58294, MAXI J1727–203 stayed close to the 1 per cent rms line while the intensity decreased. This corresponds to the softest part of the HID and the bottom left-hand part of the HRD (shown with blue triangles in the bottom panel of Figs 1 and 2). After MJD 58298, the source evolved in the opposite way going back to the right-hand side of the RID. On MJD 58302, MAXI J1727–203 crossed the 10 per cent rms line and on MJD 58310, it crossed the 20 per cent rms line. Seventeen days later, on MJD 58327, the source evolved around the 30 per cent rms line, identifying this as the AHL. This is shown with red filled crosses in Figs 1 and 2.

Fig. 4 shows three representative examples of the *NICER* PDS at three different stages of the outburst (marked in the HID and the RID as ‘PDS1’, ‘PDS2’, and ‘PDS3’, respectively). The PDS

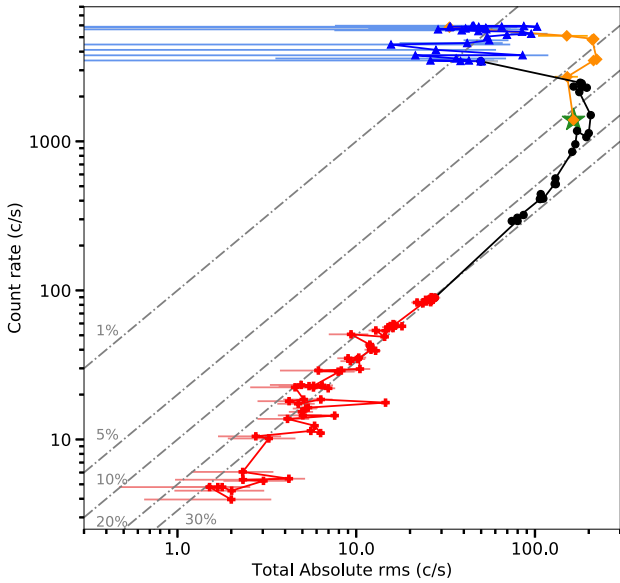


Figure 3. RID of MAXI J1727–203 during the 2018 outburst. The total absolute rms is obtained in the 0.01–64 Hz frequency range and 0.5–12 keV energy band. The count rate is obtained in the 0.5–12 keV energy band. The dashed lines represent the lines of constant fractional rms amplitude. Colours and symbols are the same as in Fig. 1. The green star marks the first *NICER* observation.

of the observations before MJD 58278 (phase A of the outburst) showed a significant broad-band noise component up to ~ 20 Hz and no significant QPOs (e.g. panel (ii) in Fig. 4). In phase B, the PDS of all the observations revealed little to no significant variability (e.g. panel (i) in Fig. 4). This corresponds to the interval plotted with blue triangles of the bottom panel of Fig. 1 and the HID and RID. Then, from MJD 58298 to the end of the outburst (phases C and D), a broad-band noise component was present with similar power-spectral shape as that in panel (ii) and panel (iii) in Fig. 4. In this period, there was significant broad-band noise extending up to a frequency of ~ 20 Hz on MJD 58298; after this date, the maximum frequency of this broad-band noise component decreased down to hundredths of Hz as the source evolved towards the end of the outburst. Fig. 5 shows the

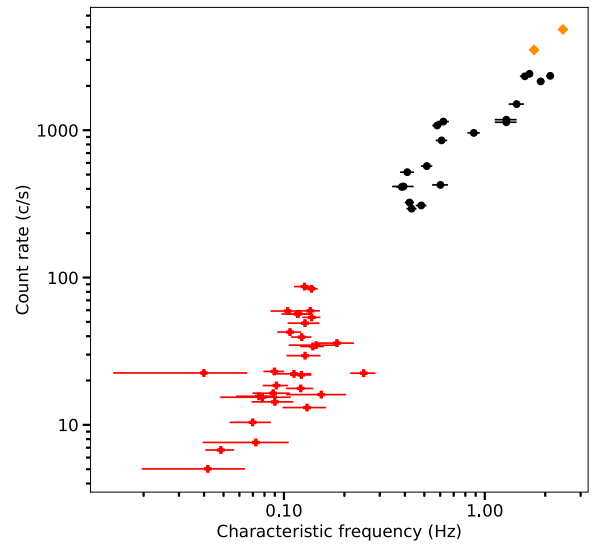


Figure 5. Characteristic frequency versus *NICER* count rate in the 0.5–12 keV energy band. Colours and symbols correspond to the phases of the outburst as described in Fig. 1.

evolution of the characteristic frequency of the broad-band noise component with intensity. We found that they are correlated.

We searched for QPOs in the PDS of MAXI J1727–203 in the 0.5–12 keV and the 2–12 keV energy bands per observation, per orbit and per region of the HID. We found evidence for QPOs in four cases: at 0.2 Hz (10.0 ± 1.6 per cent rms, ObsID 1200220134), 0.5 Hz (7.3 ± 0.7 per cent rms, ObsID 1200220127), 3 Hz (6.1 ± 0.9 per cent rms, ObsID 1200220131), and 6 Hz (1.9 ± 0.2 per cent rms, ObsID 1200220102). These QPOs are all between 3 and 3.5σ significant single trial. When considering the number of trials, these QPOs are $< 1\sigma$ significant; however, the fractional rms amplitude we measured serve as an indication of our sensitivity to detect QPOs.

Fig. 6 shows the 0.01–64 Hz fractional rms spectrum of representative observations through the whole outburst in the 0.3–12 keV energy band. The panels are chronologically ordered. The rms spectrum of panel (f) was made combining all the observations from MJD 58327 to 58346 for the same reason. From panel (a) to (e),

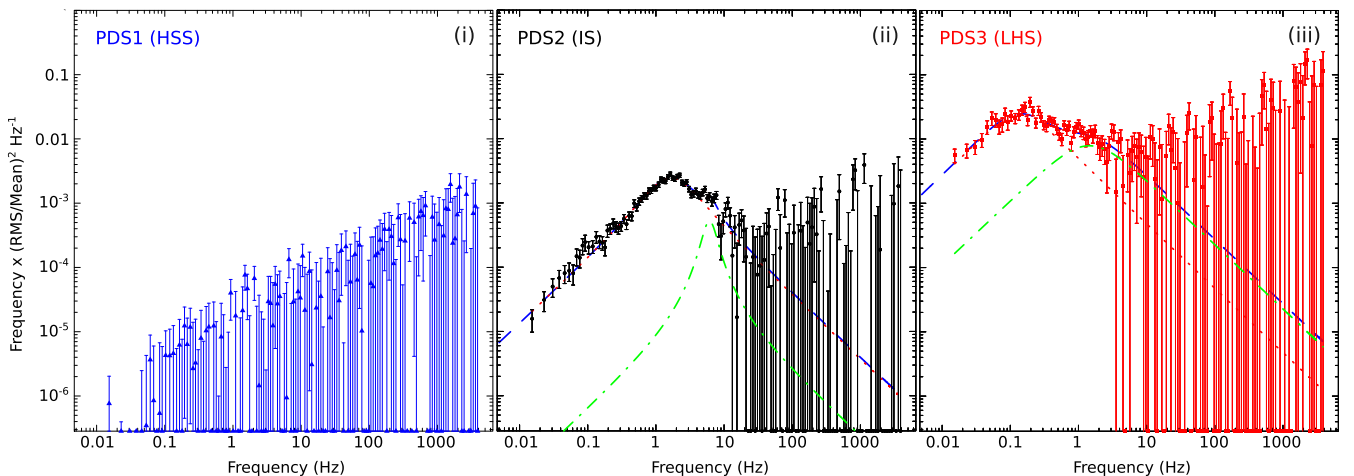


Figure 4. Three representative power spectra of the 2018 outburst of MAXI J1727–203. Panel (i) shows the power spectra of ObsID 1200220105. Panel (ii) shows the power spectra of ObsID 1200220120. Panel (iii) shows the power spectra of ObsID 1200220141. These observations occurred during phases B, C and D, respectively, of the outburst evolution. Dashed and dotted lines represent the best fit Lorentzians.

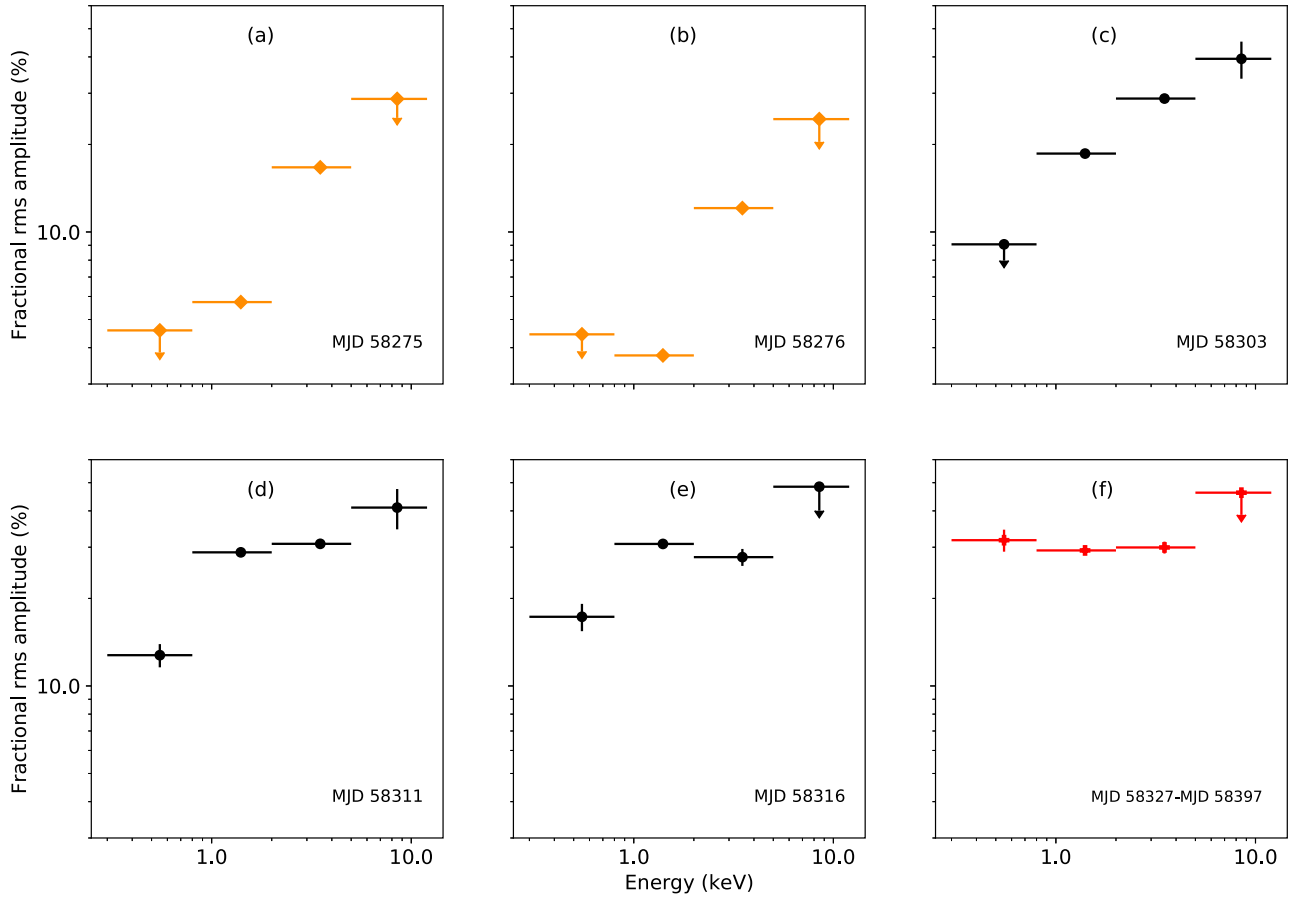


Figure 6. Evolution of the 0.01–64 Hz fractional rms spectrum of MAXI J1727–203. Plots are chronologically ordered. Colours and symbols correspond to the phases of the outburst as described in Fig. 1. Arrows represent the 95 per cent confidence upper limits of the fractional rms amplitude.

the fractional rms amplitude increased with energy. On panel (f), the fractional rms amplitude remained approximately constant with energy. During phase B of the outburst, the X-ray variability is very low, of the order of ~ 1 per cent fractional rms. We do not show the data of this phase in Fig. 6 as we only obtain upper limits in the different energy bands.

3.3 Spectral properties

We fitted the energy spectra using the model TBABS \times (NTHCOMP+DISKBB). First, we fitted all the energy spectra separately linking the kT_{seed} parameter of NTHCOMP and kT_{in} of DISKBB, and we found that the electron temperature, kT_e , in NTHCOMP was always above the maximum energy of the instrument. Therefore, we fixed kT_e at 1000 keV. Besides, we noted that the value of N_H in all the fitted energy spectra was consistent within errors. Therefore, we decided to link this parameter among all the spectra and to repeat the fitting. We obtained an average N_H of $(0.437 \pm 0.001) \times 10^{22} \text{ cm}^{-2}$ and a relatively good fit with a χ^2/dof of 1.16, for 11 107 dof (for a total of 60 spectra). The excess in χ^2 is given by the fit to some spectra, where the 5 per cent of systematic errors below 2 keV were not sufficient to mitigate the effect of instrumental residuals below 2 keV.

Fig. 7 shows four representative spectra of each phase of the outburst. The best-fitting parameters are given in Table A1, the evolution of the parameters is shown in Fig. 8. In the upper panel of Fig. 8, we show the temporal evolution of the total observed flux.

Naturally, we observed the same trend as in the upper panel of Fig. 1. In the second panel of Fig. 8, we show the temporal evolution of the Comptonised component unabsorbed flux in the 0.3–10 keV energy band. The third panel shows the contribution of the Comptonised component to the unabsorbed flux in per cent. Finally, in the last two panels, we show the temporal evolution of the photon index, Γ , of the Comptonised component and the inner disc temperature, kT_{in} , of the disc component.

The phases identified in Fig. 1 show different spectral behaviour as well, as it is shown in Fig. 8. In phase A, the contribution of the Comptonised component was ~ 20 per cent. The photon index ranged from ~ 2.5 to ~ 2.7 and the disc temperature was close to ~ 0.4 keV. The flux of the Comptonised component was $\sim 30.0 \times 10^{-10} \text{ erg cm}^{-2} \text{ s}^{-1}$. The flux of the disc component, on the other hand, ranged from $\sim 95 \times 10^{-10}$ to $\sim 135 \times 10^{-10} \text{ erg cm}^{-2} \text{ s}^{-1}$. This phase corresponds to the regions with orange diamonds in Figs 2 and 3. In phase B, the Comptonised flux dropped to $\sim 8 \times 10^{-10} \text{ erg cm}^{-2} \text{ s}^{-1}$ and decreased until $\sim 4 \times 10^{-10} \text{ erg cm}^{-2} \text{ s}^{-1}$ on MJD 58294 and, as a consequence, the contribution of the Comptonised component decreased to ~ 4 per cent. The photon index varied from ~ 2.7 to ~ 3.1 and the disc temperature decreased from ~ 0.45 to ~ 0.3 keV. This phase corresponds to the region plotted with blue triangles in the HID and the interval with lower fractional rms amplitude in the bottom panel of Figs 1 and 3 (also plotted with blue triangles on the RID). In phase C, the contribution of the Comptonised component was higher than

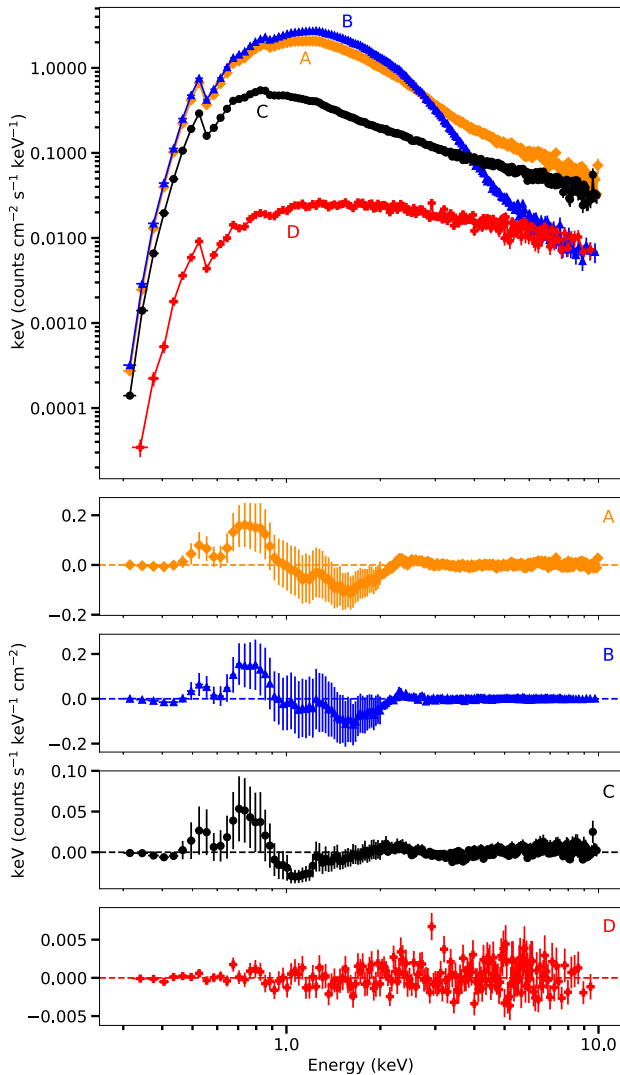


Figure 7. Upper panel: Representative energy spectra corresponding to the different phases of the outburst. Colours and symbols represent the different phases as described in Fig. 1. Dashed lines represent the best fit model in each case. Panel A, B, C, and D: residuals of the energy spectra corresponding to observations of phase A, phase B, phase C, and phase D of the outburst, respectively.

in the previous phase. At the beginning of the phase, the contribution of the Comptonised component was ~ 25 per cent and increased up to ~ 40 per cent. The photon index and the disc temperature decreased from ~ 2.5 to ~ 2.0 and from ~ 0.3 to ~ 0.15 keV, respectively. This region corresponds to the black circles in the HID and the RID, where the hardness ratio and the fractional rms amplitude increased again. Finally, in phase D, the contribution of the Comptonised component to the total unabsorbed flux was higher than 80 per cent, with the disc component becoming insignificant (i.e. not statistically required) after MJD 58342. The photon index and the disc temperature remained approximately constant around ~ 1.8 and ~ 0.1 keV, respectively. This phase corresponds to the red filled crosses of the HID and the RID. In these phases, the hardness ratio and the fractional rms amplitude remained constant at their highest values.

Our spectral modelling did not require the addition of a line-component in the 6–7 keV region. The addition of a Gaussian in this energy range led to non-physical results (the Gaussian component

became too broad and the NTHCOMP component changed). If the sigma parameter of the line was fixed to the arbitrary value of 0.3, we found that in some cases there was a significant line. In phases A and C, we could find emission lines at ~ 6.5 keV at a significance of no more than 4σ and an equivalent width of ~ 0.09 keV. After averaging all data of phase D in the period MJD 58327–58340, we were able to find a $\sim 3\sigma$ emission line at ~ 6.5 keV and an equivalent width of ~ 0.05 keV (in this case, the sigma parameter was also fixed to 0.3). These results suggest the potential presence of an emission line; however, our results are not conclusive.

In Fig. 9, we plot the fractional rms amplitude versus the flux of the disc component (left-hand panel) and the fractional rms amplitude versus the flux of the Comptonised component (right-hand panel). In the left-hand panel of Fig. 9, as the disc flux increases, the fractional rms amplitude initially remains constant, phase D, and then decreases as the disc flux increases further, C, A, and B. While during phase B the rms amplitude is consistent with being constant, those measurements are consistent with the overall trend of the rms amplitude with disc flux, and extend the anticorrelation shown by the measurements in phases C and A. On the contrary, when we plot the rms amplitude versus the Comptonised flux (right-hand panel of Fig. 9), the relation is not continuous since in those cases phase B is in between phase D and C (see Fig. 8).

4 DISCUSSION

In this paper, we present a detailed spectral and timing study of the 2018 outburst of MAXI J1727–203. We found that the system showed three different spectral states during this outburst. Fitting the energy spectra of the source with a combination of a soft thermal component and a hard Comptonised component, we found that the photon index ranges between ~ 1.75 and ~ 3.1 and the temperature at the inner disc radius ranged between 0.1 and 0.45 keV. From MJD 58342 until the end of the outburst, the disc component is not detected. The power spectra of MAXI J1727–203 showed broad-band noise up to ~ 20 Hz, without any significant QPOs. The 0.01–64 Hz averaged fractional rms amplitude (0.5–12 keV) ranged from <1 to ~ 30 per cent. In addition, we found that the fractional rms amplitude increased with energy during most of the outburst, except at the end of the outburst when it remained approximately constant with energy. All these properties allow us to discuss the nature of the compact object of MAXI J1727–203 and to determine the spectral states that characterise the source during the outburst.

Before comparing our results with previous works, it is important to note that *NICER* observations are sensitive in the 0.5–12 keV range, whereas most of our understanding of LMXBs in the last two decades comes from observations done with the Principal Counter Array (PCA) in *Rossi X-ray Timing Explorer* (*RXTE*; Bradt, Rothschild & Swank 1993), which was more sensitive in the 3–25 keV range. *NICER* observations therefore will be more affected by the interstellar absorption (which affects mainly the spectrum <3 keV) than those of *RXTE*, affecting not only the energy spectra but also the colours/hardness estimated from them. Especially important is as well the role of the disc component of the spectra on the amplitude of the variability we detect (Uttley et al. 2011). This is especially important for QPOs, but can also affect the broad-band noise. So, for example, the integrated rms amplitudes we report in the previous section are likely underestimated as compared to those we would have measured in the usual *RXTE* 3–25 keV energy band-pass. For this work, the difference in energy range probably had an impact on the q-shape loops in the HIDs and RID, as well as the correlations seen in the HRD. In the comparisons below, we at first neglect the

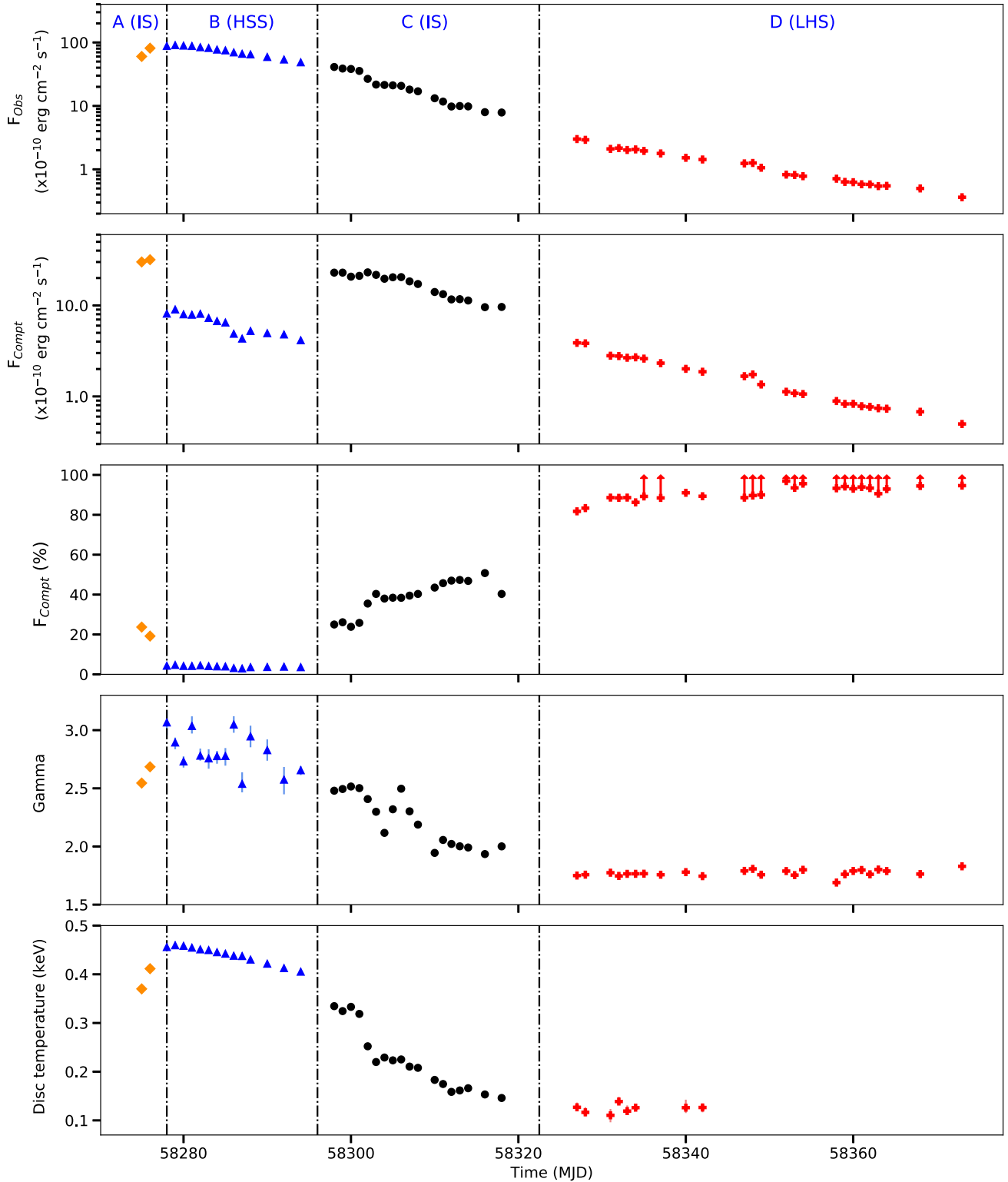


Figure 8. Evolution of the spectral parameters of MAXI J1727–203 in the 0.3–10 keV energy band. We fit *NICER* X-ray spectra using a TBABS×(NTHCOMP+DISKBB) model. From top to bottom, we plot the total observed flux, the unabsorbed Comptonised flux (F_{Compt}), the contribution of the Comptonised component to the total unabsorbed flux [F_{Compt} (per cent)], the photon index of NTHCOMP, and the temperature at the inner disc radius of DISKBB. After MJD 58342, the DISKBB component is not statistically required. The values of F_{Compt} (per cent) after MJD 58342 are not 100 per cent as those take into account the contribution to the flux of a disc (at 95 per cent upper limits). The red arrows on the third panel represent the lower limits of the F_{Compt} (per cent) in observations where the disc was not significantly detected. The different colours represent the different phases of the outburst as defined in the previous figures. The dashed line points separate the different phases.

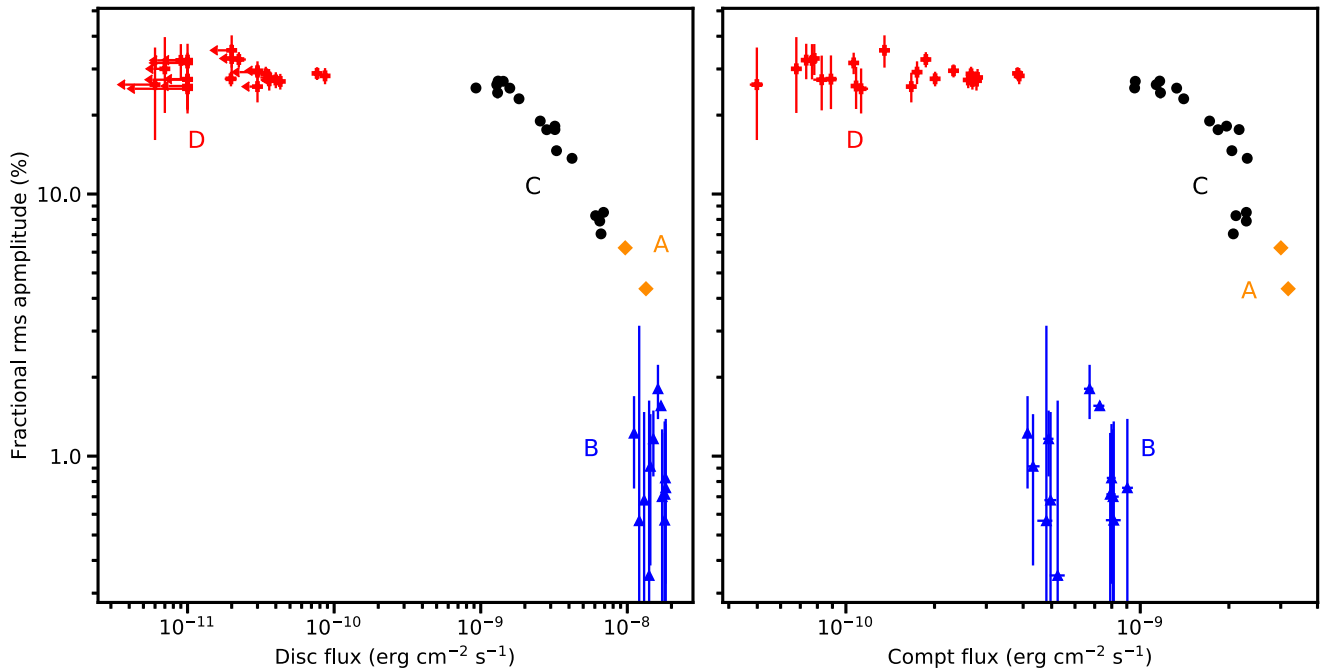


Figure 9. Plot of the 0.01–64 Hz fractional rms amplitude (0.5–12 keV) versus the flux of the disc component for MAXI J1727–203. Colours and symbols represent the different phases of the outburst as in the previous plots. Red arrows represent the 95 per cent upper limits of the disc flux.

energy range difference as we compare our results with those based on *RXTE* data but then compare it with recent results based on *NICER* observations. Our conclusions are not affected by the difference in the energy range used.

4.1 Nature of the compact object in MAXI J1727–203

The nature of the compact object in MAXI J1727–203 is still under debate. Negoro et al. (2018) suggested that the source is a BH LMXB. However, the dynamical mass of the system has not been estimated yet and the lack of very clear NS signatures (i.e. X-ray pulsations and thermonuclear X-ray bursts) does not allow to determine with absolute certainty the nature of the compact object. Below, we use the evolution of the spectral and timing properties to investigate whether the compact object is a BH or an NS.

The track traced by MAXI J1727–203 in the HID appears to trace part of the q-track, although we missed the rising part of the outburst. This hysteresis loop is typical of BH LMXBs (e.g. Homan & Belloni 2005; Remillard & McClintock 2006; Fender et al. 2009, and references therein). However, hysteresis loops have also been observed in NS LMXBs (Körding et al. 2008; Muñoz-Darias et al. 2014).

An evolution in the HRD, similar to that of MAXI J1727–203, has been observed in other LMXBs. The track we found for MAXI J1727–203 is similar to the one showed by GX 339–4 (Belloni et al. 2005) and MAXI J1348–630 (Zhang et al., in preparation), both BH LMXBs. Nevertheless, similar tracks were observed in two NS LMXBs (Aql X–1 and 4U 1705–44; Muñoz-Darias et al. 2014).

The track that MAXI J1727–203 traced in the RID is similar to the track traced by the data of the BH candidate GX 339–4 (based on *RXTE*; Muñoz-Darias et al. 2011) and MAXI J1348–630 (based on *NICER* data; Zhang et al., in preparation). The difference between MAXI J1727–203 and GX 339–4 is that the AHL of the latter was located between 30 and 40 per cent fractional rms amplitude, whereas in the case of MAXI J1727–203, the AHL line was located between

20 and 30 per cent fractional rms. Muñoz-Darias et al. (2014) found that NS LMXBs also show hysteresis in the RID. In particular, these authors found that low accretion rate NS LMXBs traced similar tracks in the RID as those traced by BH LMXBs. The main difference between these low accretion rate NS systems and BH systems is that the track followed during the state transitions is diagonal in NS, while state transitions in BH are usually horizontal, at least for low-inclination systems (Muñoz-Darias et al. 2013). This makes low accretion rate NS brighter during the soft than during the hard or intermediate states in the 3–15 keV energy band, as opposed to low-inclination BH LMXBs (Muñoz-Darias et al. 2013). In Figs 2 and 3, it is observed that, unlike the transitions found by Muñoz-Darias et al. (2014), the transition from the right-hand to the left-hand part of the diagrams are horizontal, suggesting a BH nature for MAXI J1727–203.

The X-ray timing properties of MAXI J1727–203 do not allow us to determine the nature of the compact object in the system due to the lack of specific BH and NS signatures. The presence of kHz QPOs or X-ray pulsations and type-A, B, and C QPOs would have allowed us to identify the compact object as an NS or a BH, respectively. Unfortunately, no kHz QPOs or X-ray pulsations are observed in the PDS of MAXI J1727–203. We found some marginally significant QPOs in the PDS at low frequencies (from 0.2 to 6 Hz); however the data are not sufficient to identify them with the NS or BH QPO counterparts. We can focus on the maximum frequency of the variability of the broad-band noise component. MAXI J1727–203 showed broad-band noise component that extends up to 20 Hz. Based on the results of Sunyaev & Revnivtsev (2000), this behaviour is more typical of BHs, since the power spectra of BH LMXBs display a strong decline at frequencies higher than 10–50 Hz, with no significant variability above 100–200 Hz (e.g. GX 339–4, GS 1354–644, XTE J1748–288, and 4U 1630–47). NS LMXBs, on the other hand, can show significant variability in the power spectra up to 500–1000 Hz (e.g. 4U 1608–522, SAX J1808.4–3658, and 4U 0614+091). The fact that MAXI J1727–203 showed variability only up to

20 Hz suggests that the compact object in MAXI J1727–203 is a BH.

The evolution of the energy dependence of the fractional rms amplitude of the broad-band noise component at energies 0.3–12 keV is consistent with what has been seen in other BH LMXBs in energies above 2–3 keV (e.g. XTE J1550–564 and XTE J1650–50; Gierliński & Zdziarski 2005). We found that during most of the outburst, the fractional rms amplitude increased with energy. The only exception is shown in the panel (f) of Fig. 6 where the rms remained approximately constant with energy. This panel corresponds to the spectrally hardest observations in Figs 2 and 3 (red crosses of the diagrams). Gierliński & Zdziarski (2005) found that in the hard state of XTE J1550–564 and XTE J1650–50 the rms-spectra remained constant or slightly decreased with energy, while in the intermediate and the soft state the rms spectra increased with energy. Some NS show a similar behaviour (e.g. XTE J1701–462; Bu et al. 2015). The rms spectra of broad-band noise components of NS increase with energy in some cases (Bu et al. 2015; Bult 2017, studying XTE J1701–462 and MAXI J0911–655, respectively), as MAXI J1727–203 did during most of the outburst. Unfortunately, neither of those works present the evolution of the rms spectra during a whole outburst, so at the moment we cannot compare the evolution of these sources and that of MAXI J1727–203.

The evolution of the spectral parameters of MAXI J1727–203 is similar to what has been observed in other BH LMXBs and NS LMXBs. The photon index of MAXI J1727–203 ranged from ~ 1.75 to ~ 3.1 . This evolution is similar to two of the most studied BH LMXBs, Cyg X–1 (photon index from ~ 1.5 to ~ 2.7 ; Titarchuk 1994) and GX 339–4 (photon index from ~ 1.5 to ~ 2.9 ; Plant et al. 2014). We also compared the photon index of MAXI J1727–203 with the photon index of two NS LMXBs: 4U 1636–53 and MXB 1658–298 during its 2015–2017 outburst. In the case of 4U 1636–53, the photon index ranged from 1.3 to 2.5 (Zhang et al. 2017). This range is similar to the photon index range of MAXI J1727–203. In the case of MXB 1658–298, the photon index ranged from ~ 1.7 to ~ 2.4 (Sharma et al. 2018). Although the photon index in NS LMXBs might show lower values than for BH LMXBs (something that would have to be tested studying a much larger sample), this potential difference would argue that MAXI J1727–203 is a BH candidate. In terms of the inner disc temperature, MAXI J1727–203 showed a lower temperature than other BH LMXBs. The disc temperature of GX 339–4 ranged from ~ 0.6 to ~ 0.9 keV (Plant et al. 2014) and the temperature of Cyg X–1 ranged between 0.5 and 0.6 keV (Shaposhnikov & Titarchuk 2006). The temperature of 4U 1636–53 ranged from ~ 0.3 to ~ 0.8 keV in the best-fitting results (Zhang et al. 2017) and the disc temperature of MXB 1658–298 ranged from ~ 0.6 to ~ 0.9 keV (Sharma et al. 2018). The disc temperature of MAXI J1727–203 was lower than these four systems.

A potential explanation for a lower temperature in MAXI J1727–203 than in other sources could be related to the mass of the compact object. Assuming that the accretion disc is at the innermost stable circular orbit (ISCO), the temperature at the inner disc radius is proportional to $(\dot{M}/M^2)^{1/4}$, where \dot{M} is the mass accretion rate and M is the mass of the compact object (Frank, King & Raine 2002). According to Muñoz-Darias, Casares & Martínez-Pais (2008), $M < 6 M_{\odot}$ for GX 339–4. We take the temperature of GX 339–4 in the soft state (0.79 keV) from Plant et al. (2014) and we also take the disc temperature of the softest observation in the HID of MAXI J1727–203 (0.45 keV). From that, if we assume that \dot{M} is the same for two sources in the same spectral state, we estimate a lower limit for the mass of MAXI J1727–203 of $\sim 19 M_{\odot}$. Therefore, the high mass of the compact object can explain the low temperature of the

inner disc. Alternatively, as suggested by Gou et al. (2011), the low temperature at the inner disc radius can be a consequence of a low inclination of the accretion disc with respect to the line of sight.

We can repeat this analysis to estimate the mass of MAXI J1727–203 with the NS Aql X–1. For this, we took the temperature of Aql X–1 in the soft state of its 2007 outburst (~ 0.66 keV, Raichur, Misra & Dewangan 2011). Considering a mass of $\sim 1.4 M_{\odot}$ for the NS in Aql X–1, we obtained a mass of $\sim 2 M_{\odot}$ for the compact object in MAXI J1727–203. If we consider a higher mass for Aql X–1, the mass of MAXI J1727–203 also increases. Considering the latter, this mass estimates suggest that the compact object in MAXI J1727–203 is massive NS or a low-mass BH.

Based on all the above comparisons, although we cannot unambiguously identify the nature of the compact object in MAXI J1727–203, the evolution in the HID, RID, and RHD, and the temperature at the inner radius of the accretion disc during the softest observations suggest that it is a BH.

4.2 Anticorrelation between the fractional rms amplitude and the flux of the disc component

Fig. 9 shows that the relation between the fractional rms amplitude and the disc flux is continuous and that both quantities are anticorrelated during phases A and C (orange diamonds and black circles) of the outburst. While in phases B and D (blue triangles and red crosses), the rms amplitude is consistent with being independent of the disc flux, those measurements extend the relation seen in phases A and C to low (phase D) and high (phase B) values of the disc flux.

The simplest interpretation of this behaviour is that the variability is produced by the Comptonised component, the disc emission is not variable, and as the relative contribution of the disc to the total emission increases, the variability decreases. If this is the case, the intrinsic variability would be produced by the corona (e.g. for QPOs; Lee & Miller 1998; Lee, Misra & Taam 2001; Kumar & Misra 2014). Karpouzas et al. (2020) explain this for the kHz QPOs in neutron-star LMXBs, and Zhang et al. (2020) for the type C QPOs in the BH candidate GRS 1915+105, but the same mechanism could apply for the broad-band component that we discuss here. A similar argument was discussed by Méndez, van der Klis & Ford (2001) for the dependence of the rms amplitude of the kHz QPOs in the neutron-star LMXBs 4U 1728–34, 4U 1608–52, and Aql X–1.

4.3 Spectral states of MAXI J1727–203

Assuming that the source is a BH LMXB, we can identify its spectral states from its spectral and timing properties. Here, we describe the different spectral states found for MAXI J1727–203:

(i) Low/hard state (LHS): From MJD 58327 to 58397. This period corresponds to phase D of the outburst marked with red filled crosses in Figs 1, 2, 3, 8, and 9. In the HID, the source was in the right vertical branch with hardness values close to ~ 0.1 . The fractional rms amplitude in the LHS state was close to ~ 30 per cent and followed the AHL in the RID, supporting the LHS classification state based on the results of Muñoz-Darias et al. (2011). The fractional rms amplitude was also approximately constant with energy (panel with red filled crosses in Fig. 6). The PDS was dominated by a broad-band noise component [panel (iii) in Fig. 4]. In terms of spectral properties, the contribution of the Comptonised component was > 80 per cent in this state. At the end of the outburst, the disc component is not significant.

The fractional rms amplitude is not correlated with the flux of the Comptonised component. This is because the fractional rms remains approximately constant with energy. The photon index of the Comptonised component and the inner disc temperature remained approximately constant at ~ 1.8 and ~ 0.1 keV, respectively.

(ii) Intermediate states (IS): From MJD 58274 to 58278 and from MJD 58298 to 58327. These periods correspond to phases A and C of the outburst, respectively, which are marked with orange diamonds (phase A) and black circles (phase C) in Figs 1, 2, 3, 8, and 9. In the HID, these correspond to the horizontal branches with hardness values from ~ 0.02 to ~ 0.1 . In these periods, the fractional rms amplitude ranged from ~ 5 to ~ 30 per cent and the source evolved to the top left-hand part of the RID in the first epoch (MJD 58274–58278) and to the AHL in the second epoch (MJD 58298–58327), as can be seen in Fig. 3. The fractional rms amplitude increased with energy (panels with black circles and orange diamonds in Fig. 6) and the PDS was dominated by a broad-band noise component [panel (ii) in Fig. 4]. No significant QPOs are detected during this phase. The characteristic frequency also increases with the intensity. The contribution of the Comptonised component ranged from ~ 20 to 50 per cent. The fractional rms amplitude and the flux of the Comptonised flux are anticorrelated, suggesting that the change of variability is driven by changes in the flux of the Comptonised component. The photon index of the Comptonised component in this state ranged from ~ 2.0 to ~ 2.7 and the inner disc temperature decreased from ~ 0.4 to ~ 0.15 keV.

(iii) High/soft state (HSS): From MJD 58278 to 58298. This period corresponds to phase B of the outburst, plotted with blue triangles in Figs 1, 2, 3, 8, and 9. In the HID, the hardness ratio was approximately constant close to ~ 0.005 . The fractional rms amplitude was ~ 1 per cent, which can be observed in the top left-hand part of the RID, where the source evolved around the 1 per cent fractional rms line. The maximum frequency also increases with energy. The rms spectrum increases with energy (blue triangles in Fig. 6). The contribution of the Comptonised component was less than 5 per cent, the photon index of the Comptonised component ranged from ~ 2.5 to ~ 3.0 and the temperature of the inner disc decreased from ~ 0.45 to ~ 0.3 keV. The rms–flux correlation was flat with some scatter (Fig. 9).

ACKNOWLEDGEMENTS

This work is based on observations made by the *NICER* X-ray mission supported by NASA. This research has made use of data and software provided by the High Energy Astrophysics Science Archive Research Center (HEASARC), a service of the Astrophysics Science Division at NASA/GSFC and the High Energy Astrophysics Division of the Smithsonian Astrophysical Observatory. This research has made use of the *MAXI* light curve provided by RIKEN, JAXA, and the *MAXI* team. This research has also made use of *Swift*/BAT transient monitor results provided by the *Swift*/BAT team. KA acknowledges support from a UGC–UKIERI Phase 3 Thematic Partnership (UGC–UKIERI-2017-18-006; PI: P. Gandhi). KA especially acknowledges Dr. Keith Arnaud for his help with the X-ray tool XSPEC. DA and DJKB acknowledge support from the Royal Society. VAC acknowledges support from the Royal Society International Exchanges ‘The first step for High-Energy Astrophysics relations between Argentina and UK’ and from the Spanish Ministerio de Ciencia e Innovación under grant AYA2017-83216-P. LZ and AC acknowledge support from the Royal Society Newton International Fellowship. RML acknowledges the support of NASA through Hubble Fellowship Program grant HST-HF2-51440.001.

DATA AVAILABILITY

The data underlying this article are publicly available in the High Energy Astrophysics Science Archive Research Center (HEASARC) at <https://heasarc.gsfc.nasa.gov/db-perl/W3Browse/w3browse.pl>

REFERENCES

- Arnaud K. A., 1996, in Jacoby G. H., Barnes J., eds, *ASP Conf. Ser. Vol. 101, Astronomical Data Analysis Software and Systems V*. Astron. Soc. Pac., San Francisco, p. 17
- Belloni T., Homan J., Casella P., van der Klis M., Nespoli E., Lewin W. H. G., Miller J. M., Méndez M., 2005, *A&A*, 440, 207
- Belloni T., Psaltis D., van der Klis M., 2002, *ApJ*, 572, 392
- Belloni T. et al., 2006, *MNRAS*, 367, 1113
- Belloni T. M., 2010, in Belloni T., ed., *Lecture Notes in Physics*, Vol. 794, The Jet Paradigm. Springer-Verlag, Berlin, p. 53
- Belloni T. M., Stella L., 2014, *Space Sci. Rev.*, 183, 43
- Belloni T. M., Motta S. E., Muñoz-Darias T., 2011, *Bull. Astron. Soc. India*, 39, 409
- Bradt H. V., Rothschild R. E., Swank J. H., 1993, *A&AS*, 97, 355
- Bult P., 2017, *ApJ*, 837, 61
- Bu Q.-c., Chen L., Li Z.-s., Qu J.-l., Belloni T. M., Zhang L., 2015, *ApJ*, 799, 2
- Burke M. J., Gilfanov M., Sunyaev R., 2017, *MNRAS*, 466, 194
- Capitanio F., Belloni T., Del Santo M., Ubertini P., 2009, *MNRAS*, 398, 1194
- Casella P., Belloni T., Homan J., Stella L., 2004, *A&A*, 426, 587
- Di Salvo T. et al., 2000, *ApJ*, 544, L119
- Done C., Gierliński M., 2003, *MNRAS*, 342, 1041
- Done C., Gierliński M., Kubota A., 2007, *Astron. Astrophys. Rev.*, 15, 1
- Dunn R. J. H., Fender R. P., Körding E. G., Belloni T., Cabanac C., 2010, *MNRAS*, 403, 61
- Fender R. P., Homan J., Belloni T. M., 2009, *MNRAS*, 396, 1370
- Frank J., King A., Raine D. J., 2002, *Accretion Power in Astrophysics*, 3rd edn. Cambridge Univ. Press, Cambridge
- Gao H. Q. et al., 2017, *MNRAS*, 466, 564
- Gehrels N. et al., 2004, *ApJ*, 611, 1005
- Gendreau K. C., Arzoumanian Z., Okajima T., 2012, in Takahashi T., Murray S. S., Herder J.-W. A. den, eds, *Proc. SPIE Conf. Ser. Vol. 8443, Space Telescopes and Instrumentation 2012: Ultraviolet to Gamma Ray*. SPIE, Bellingham, p. 844313
- Gierliński M., Done C., 2002, *MNRAS*, 337, 1373
- Gierliński M., Zdziarski A. A., 2005, *MNRAS*, 363, 1349
- Gou L. et al., 2011, *ApJ*, 742, 85
- Hasinger G., van der Klis M., 1989, *A&A*, 225, 79
- Homan J., Belloni T., 2005, *Ap&SS*, 300, 107
- Homan J., Wijnands R., van der Klis M., Belloni T., van Paradijs J., Klein-Wolt M., Fender R., Méndez M., 2001, *ApJS*, 132, 377
- Karpouzas K., Méndez M., Ribeiro E. r. M., Altamirano D., Blaes O., García F., 2020, *MNRAS*, 492, 1399
- Kennea J. A., Bahramian A., Beardmore A. P., 2018, *Astron. Telegram*, 11697
- Klein-Wolt M., van der Klis M., 2008, *ApJ*, 675, 1407
- Kumar N., Misra R., 2014, *MNRAS*, 445, 2818
- Körding E., Rupen M., Knigge C., Fender R., Dhawan V., Templeton M., Muxlow T., 2008, *Science*, 320, 1318
- Leahy D. A., Darbro W., Elsner R. F., Weisskopf M. C., Sutherland P. G., Kahn S., Grindlay J. E., 1983, *ApJ*, 266, 160
- Lee H. C., Miller G. S., 1998, *MNRAS*, 299, 479
- Lee H. C., Misra R., Taam R. E., 2001, *ApJ*, 549, L229
- Lin D., Remillard R. A., Homan J., 2007, *ApJ*, 667, 1073
- Ludlam R. M. et al., 2018a, *ApJ*, 858, L5
- Ludlam R. M. et al., 2018b, *Astron. Telegram*, 11689
- Krimm H. A. et al., 2013, *APJS*, 209, 14
- Matsuoka M. et al., 2009, *PASJ*, 61, 999
- Miller J. M. et al., 2018, *ApJ*, 860, L28
- Mitsuda K. et al., 1984, *PASJ*, 36, 741
- Miyamoto S., Kitamoto S., Hayashida K., Egoshi W., 1995, *ApJ*, 442, L13

- Motta S., Homan J., Muñoz Darias T., Casella P., Belloni T. M., Hiemstra B., Méndez M., 2012, *MNRAS*, 427, 595
- Motta S. E., 2016, *Astron. Nachr.*, 337, 398
- Muñoz-Darias T., Casares J., Martínez-Pais I. G., 2008, *MNRAS*, 385, 2205
- Muñoz-Darias T., Motta S., Belloni T. M., 2011, *MNRAS*, 410, 679
- Muñoz-Darias T., Coriat M., Plant D. S., Ponti G., Fender R. P., Dunn R. J. H., 2013, *MNRAS*, 432, 1330
- Muñoz-Darias T., Fender R. P., Motta S. E., Belloni T. M., 2014, *MNRAS*, 443, 3270
- Méndez M., van der Klis M., 1997, *ApJ*, 479, 926
- Méndez M., van der Klis M., Ford E. C., 2001, *ApJ*, 561, 1016
- Negoro H. et al., 2018, *Astron. Telegram*, 11696
- Plant D. S., Fender R. P., Ponti G., Muñoz-Darias T., Coriat M., 2014, *MNRAS*, 442, 1767
- Raichur H., Misra R., Dewangan G., 2011, *MNRAS*, 416, 637
- Remillard R. A., McClintock J. E., 2006, *ARA&A*, 44, 49
- Shakura N. I., Sunyaev R. A., 1973, in Bradt H., Giacconi R., eds, *Proc. IAU Symp. 55, X- and Gamma-Ray Astronomy*. Reidel, Dordrecht, p. 155
- Shaposhnikov N., Titarchuk L., 2006, *ApJ*, 643, 1098
- Sharma R., Jaleel A., Jain C., Pandey J. C., Paul B., Dutta A., 2018, *MNRAS*, 481, 5560
- Sunyaev R., Revnivtsev M., 2000, *A&A*, 358, 617
- Sunyaev R. A., Titarchuk L. G., 1980, *A&A*, 86, 121
- Sunyaev R. A., Truemper J., 1979, *Nature*, 279, 506
- Tanaka Y., 1989, in Hunt J., Battrick B., eds, *ESA SP-296: Two Topics in X-Ray Astronomy: Vol. 1 X Ray Binaries and Vol. 2 AGN and the X Ray Background*. ESA, Noordwijk, p. 3
- Titarchuk L., 1994, *ApJ*, 434, 570
- Tomsick J., Shaw A., Garcia J., Walton D., Fuerst F., Miller J., Parker M., Xu Y., 2018, *Astron. Telegram*, 11881
- Uttley P., Klein-Wolt M., 2015, *MNRAS*, 451, 475
- Uttley P., Wilkinson T., Cassatella P., Wilms J., Pottschmidt K., Hanke M., Böck M., 2011, *MNRAS*, 414, L60
- van der Klis M., 1989, *ARA&A*, 27, 517
- van der Klis M., 1994, *ApJS*, 92, 511
- van der Klis M., 1995, in Alpar M. A., Kiziloglu U., van Paradijs J., eds, *NATO ASI Ser. C Vol. 450, The Lives of the Neutron Stars*. Kluwer, Dordrecht, p. 301
- van der Klis M., 2000, *ARA&A*, 38, 717
- van der Klis M., 2006, *Compact Stellar X-ray Sources*, Cambridge Univ. Press, Cambridge
- van Doesburgh M., van der Klis M., Morsink S. M., 2018, *MNRAS*, 479, 426
- Verner D. A., Ferland G. J., Korista K. T., Yakovlev D. G., 1996, *ApJ*, 465, 487
- Wang-Ji J. et al., 2018, *ApJ*, 855, 61
- Wijnands R., Homan J., van der Klis M., 1999, *ApJ*, 526, L33
- Wilms J., Allen A., McCray R., 2000, *ApJ*, 542, 914
- Yoneyama T. et al., 2018, *Astron. Telegram*, 11683
- Zdziarski A. A., Gierliński M., 2004, *Prog. Theor. Phys. Suppl.*, 155, 99
- Zdziarski A. A., Johnson W. N., Magdziarz P., 1996, *MNRAS*, 283, 193
- Zhang G., Méndez M., Sanna A., Ribeiro E. M., Gelfand J. D., 2017, *MNRAS*, 465, 5003
- Zhang L. et al., 2020, *MNRAS*, 494, 1375
- Życk P. T., Done C., Smith D. A., 1999, *MNRAS*, 309, 561

APPENDIX A: SPECTRAL FITTING PARAMETERS

Table A1. Summary of the spectral parameters of MAXI J1727–203 in the 0.3–10 keV energy band. Errors represent the 1σ level confidence interval of the parameter. For the observations in which we do not detect the disc component significantly, we give the 95 per cent confidence upper limit of the disc normalisation and the corresponding disc flux.

MJD	Γ	NTHCOMP normalisation ($\times 10^{-2}$)	kT_{in} (keV)	DISKBB normalisation [$\times 10^4 \text{ km}^2$ (10kpc) $^{-2}$]	Comptonised flux ($\times 10^{-10} \text{ erg cm}^{-2} \text{ s}^{-1}$)	Disc flux ($\times 10^{-10} \text{ erg cm}^{-2} \text{ s}^{-1}$)	Unabsorbed flux ($\times 10^{-10} \text{ erg cm}^{-2} \text{ s}^{-1}$)	Total absorbed flux ($\times 10^{-10} \text{ erg cm}^{-2} \text{ s}^{-1}$)	Phase
NICER									outburst
58275	2.53 ± 0.03	50.9 ± 0.1	0.370 ± 0.001	2.99 ± 0.03	30.0 ± 0.3	$96.7^{+0.6}_{-1.0}$	$126.8^{+0.7}_{-1.0}$	60.2 ± 0.2	A
58276	2.68 ± 0.03	50.5 ± 0.2	0.412 ± 0.003	2.62 ± 0.08	31.8 ± 0.5	134.0 ± 0.9	166 ± 1	$81.3^{+0.4}_{-0.3}$	A
58278	3.1 ± 0.1	12.7 ± 0.1	0.456 ± 0.002	2.28 ± 0.04	8.1 ± 0.5	179.8 ± 0.4	187.9 ± 0.6	$88.00^{+0.09}_{-0.06}$	B
58279	2.89 ± 0.05	13.3 ± 0.1	0.459 ± 0.002	2.24 ± 0.04	9.0 ± 0.4	183.0 ± 0.8	192.0 ± 0.8	90.7 ± 0.3	B
58280	2.73 ± 0.05	11.1 ± 0.1	0.458 ± 0.002	2.26 ± 0.04	8.0 ± 0.3	181.7 ± 0.9	189.8 ± 0.9	89.3 ± 0.4	B
58281	3.04 ± 0.07	12.33 ± 0.08	0.455 ± 0.001	2.32 ± 0.02	7.9 ± 0.3	181.0 ± 0.8	188.4 ± 0.9	88.0 ± 0.3	B
58282	2.78 ± 0.05	11.71 ± 0.09	0.451 ± 0.002	2.29 ± 0.04	8.1 ± 0.4	173.0 ± 0.8	181.0 ± 0.8	84.2 ± 0.3	B
58283	2.76 ± 0.09	10.5 ± 0.1	0.449 ± 0.002	2.28 ± 0.04	7.3 ± 0.4	169.6 ± 0.8	176.9 ± 0.9	81.9 ± 0.3	B
58284	$2.78^{+0.04}_{-0.07}$	9.90 ± 0.09	0.445 ± 0.001	2.27 ± 0.02	6.7 ± 0.3	161.8 ± 0.8	169.0 ± 0.9	77.3 ± 0.3	B
58285	2.78 ± 0.08	9.67 ± 0.07	0.442 ± 0.001	2.28 ± 0.02	6.5 ± 0.3	158.3 ± 0.4	164.8 ± 0.5	75.1 ± 0.2	B
58286	3.05 ± 0.07	8.06 ± 0.07	0.438 ± 0.001	2.27 ± 0.02	4.9 ± 0.2	150.5 ± 0.7	155.4 ± 0.7	69.8 ± 0.2	B
58287	2.54 ± 0.08	5.90 ± 0.06	0.437 ± 0.001	2.17 ± 0.02	4.3 ± 0.2	143.5 ± 0.5	147.8 ± 0.6	66.3 ± 0.1	B
58288	2.95 ± 0.09	8.57 ± 0.09	0.430 ± 0.001	2.28 ± 0.02	5.2 ± 0.3	140.8 ± 0.7	146.0 ± 0.7	64.9 ± 0.2	B
58290	2.83 ± 0.09	8.00 ± 0.08	0.421 ± 0.002	2.30 ± 0.04	5.0 ± 0.2	130.2 ± 0.7	135.1 ± 0.8	59.1 ± 0.3	B
58292	2.6 ± 0.1	7.2 ± 0.1	0.413 ± 0.002	2.34 ± 0.05	4.8 ± 0.3	121 ± 1	125 ± 1	53.9 ± 0.3	B
58294	2.66 ± 0.04	6.55 ± 0.05	0.4053 ± 0.0007	2.32 ± 0.02	4.14 ± 0.08	111.0 ± 0.6	115.2 ± 0.6	48.7 ± 0.2	B
58298	2.48 ± 0.02	42.1 ± 0.1	0.330 ± 0.001	3.29 ± 0.04	22.9 ± 0.2	68.8 ± 0.6	91.7 ± 0.6	41.1 ± 0.1	C
58299	2.49 ± 0.02	43.7 ± 0.1	0.324 ± 0.002	3.55 ± 0.09	22.9 ± 0.3	64.8 ± 0.5	87.8 ± 0.6	38.8 ± 0.1	C
58300	2.52 ± 0.02	38.9 ± 0.1	0.333 ± 0.002	3.23 ± 0.08	20.7 ± 0.2	66.2 ± 0.9	86.9 ± 0.9	38.2 ± 0.2	C
58301	2.50 ± 0.02	41.1 ± 0.1	0.319 ± 0.002	3.59 ± 0.09	21.1 ± 0.3	60.8 ± 0.4	81.9 ± 0.5	$35.60^{+0.08}_{-0.03}$	C
58302	2.41 ± 0.02	51.2 ± 0.02	0.252 ± 0.003	7.1 ± 0.3	23.1 ± 0.3	41.9 ± 0.6	65.1 ± 0.6	26.7 ± 0.1	C
58303	2.30 ± 0.01	48.3 ± 0.1	0.220 ± 0.003	10.1 ± 0.6	21.7 ± 0.2	32.1 ± 0.5	53.7 ± 0.5	21.70 ± 0.09	C
58304	2.12 ± 0.01	37.9 ± 0.1	0.229 ± 0.002	8.3 ± 0.3	19.6 ± 0.2	32.0 ± 0.4	51.7 ± 0.4	$21.40^{+0.05}_{-0.09}$	C
58305	2.32 ± 0.02	45.7 ± 0.2	0.223 ± 0.003	9.6 ± 0.5	20.4 ± 0.3	32.7 ± 0.6	53.1 ± 0.6	21.1 ± 0.1	C
58306	2.50 ± 0.02	50.6 ± 0.3	0.225 ± 0.004	9.3 ± 0.6	20.5 ± 0.3	32.9 ± 0.4	53.4 ± 0.6	20.70 ± 0.06	C
58307	2.30 ± 0.02	41.7 ± 0.2	0.210 ± 0.003	10.9 ± 0.6	18.4 ± 0.3	28.2 ± 0.4	46.6 ± 0.5	18.10 ± 0.08	C
58308	2.188 ± 0.009	36.4 ± 0.1	0.2079 ± 0.0009	10.4 ± 0.2	17.20 ± 0.08	25.5 ± 0.2	42.7 ± 0.3	17.00 ± 0.05	C
58310	1.944 ± 0.008	25.5 ± 0.1	0.183 ± 0.002	13.7 ± 0.6	14.04 ± 0.07	18.2 ± 0.2	32.3 ± 0.2	13.2 ± 0.06	C
58311	2.05 ± 0.01	26.5 ± 0.1	0.175 ± 0.002	14.9 ± 0.7	13.29 ± 0.09	15.8 ± 0.3	29.1 ± 0.3	11.70 ± 0.03	C
58312	2.02 ± 0.02	22.8 ± 0.2	0.159 ± 0.002	20 ± 1	11.64 ± 0.07	13.1 ± 0.2	24.8 ± 0.2	9.79 ± 0.08	C
58313	2.00 ± 0.02	22.6 ± 0.2	0.161 ± 0.002	18.0 ± 0.9	11.7 ± 0.1	13.0 ± 0.2	24.7 ± 0.2	9.96 ± 0.06	C
58314	1.99 ± 0.01	21.64 ± 0.08	0.166 ± 0.002	15.5 ± 0.8	11.33 ± 0.06	12.9 ± 0.3	24.2 ± 0.3	9.82 ± 0.04	C

Table A1 – *continued*

MID	Γ	NTHCOMP normalisation ($\times 10^{-2}$)	kT_{in} (keV)	DISKBB normalisation [$\times 10^4 \text{ km}^2$ (10 kpc) $^{-2}$]	Comptonised flux ($\times 10^{-10} \text{ erg cm}^{-2} \text{ s}^{-1}$)	Disc flux ($\times 10^{-10} \text{ erg cm}^{-2} \text{ s}^{-1}$)	Unabsorbed flux ($\times 10^{-10} \text{ erg cm}^{-2} \text{ s}^{-1}$)	Total absorbed flux ($\times 10^{-10} \text{ erg cm}^{-2} \text{ s}^{-1}$)	Phase outburst
<i>NICER</i>									
58316	$1.935^{+0.008}_{-0.011}$	17.53 ± 0.08	0.153 ± 0.003	17 ± 1	9.57 ± 0.07	9.3 ± 0.3	18.9 ± 0.3	7.97 ± 0.04	C
58318	2.001 ± 0.009	17.50 ± 0.09	0.146 ± 0.004	16 ± 2	9.6 ± 0.1	14 ± 1	24 ± 1	7.87 ± 0.04	C
58327	1.75 ± 0.03	6.03 ± 0.05	0.127 ± 0.008	4 ± 1	3.88 ± 0.05	0.87 ± 0.07	4.75 ± 0.08	3.00 ± 0.04	D
58328	1.76 ± 0.01	5.97 ± 0.04	0.117 ± 0.009	6 ± 2	3.83 ± 0.04	0.77 ± 0.04	4.59 ± 0.06	2.92 ± 0.03	D
58331	1.77 ± 0.02	4.42 ± 0.04	0.11 ± 0.01	4 ± 1	2.80 ± 0.06	0.36 ± 0.05	3.16 ± 0.07	2.10 ± 0.02	D
58332	1.75 ± 0.01	4.31 ± 0.03	$0.139^{+0.009}_{-0.006}$	1.1 ± 0.3	2.78 ± 0.03	0.36 ± 0.04	3.14 ± 0.05	2.16 ± 0.02	D
58333	1.77 ± 0.01	4.52 ± 0.03	0.12 ± 0.09	$2.3^{+1.0}_{-0.7}$	2.66 ± 0.03	0.34 ± 0.04	3.00 ± 0.04	$2.020^{+0.006}_{-0.010}$	D
58334	1.77 ± 0.02	4.24 ± 0.03	0.126 ± 0.007	2.1 ± 0.5	2.69 ± 0.03	0.43 ± 0.03	3.12 ± 0.04	2.06 ± 0.02	D
58335	1.77 ± 0.01	4.08 ± 0.02	–	<5	2.60 ± 0.03	<0.4	2.92 ± 0.05	1.95 ± 0.02	D
58337	1.76 ± 0.02	3.63 ± 0.02	–	<3	2.32 ± 0.05	<0.3	2.62 ± 0.05	$1.780^{+0.020}_{-0.007}$	D
58340	$1.779^{+0.011}_{-0.005}$	3.41 ± 0.02	0.13 ± 0.02	0.9 ± 0.3	2.01 ± 0.03	0.19 ± 0.02	2.20 ± 0.04	1.520 ± 0.006	D
58342	1.74 ± 0.02	2.89 ± 0.02	0.126 ± 0.009	1.1 ± 0.3	1.87 ± 0.03	0.22 ± 0.03	2.09 ± 0.04	1.43 ± 0.01	D
58347	1.79 ± 0.02	2.79 ± 0.03	–	<5	1.67 ± 0.04	<0.3	1.88 ± 0.06	1.24 ± 0.02	D
58348	$1.808^{+0.007}_{-0.012}$	2.79 ± 0.02	–	<19	1.74 ± 0.04	<0.3	1.95 ± 0.09	$1.260^{+0.010}_{-0.007}$	D
58349	1.76 ± 0.03	2.09 ± 0.03	–	<0.6	1.35 ± 0.06	<0.2	1.50 ± 0.07	1.06 ± 0.03	D
58352	1.79 ± 0.03	1.79 ± 0.02	–	<2	1.13 ± 0.05	<0.1	1.16 ± 0.07	$0.830^{+0.020}_{-0.009}$	D
58353	1.75 ± 0.01	1.68 ± 0.01	–	<2	1.08 ± 0.03	<0.1	1.16 ± 0.04	0.815 ± 0.008	D
58354	1.799 ± 0.009	1.71 ± 0.01	–	<3	1.06 ± 0.04	<0.1	1.11 ± 0.05	$0.779^{+0.009}_{-0.004}$	D
58358	1.69 ± 0.02	1.29 ± 0.01	–	<2	0.89 ± 0.04	<0.1	0.95 ± 0.05	$0.710^{+0.009}_{-0.006}$	D
58359	1.76 ± 0.04	1.30 ± 0.01	–	<0.6	0.83 ± 0.05	<0.1	0.88 ± 0.07	0.64 ± 0.01	D
58360	1.79 ± 0.02	1.33 ± 0.01	–	<0.5	0.83 ± 0.03	<0.1	0.89 ± 0.04	0.627 ± 0.007	D
58361	1.79 ± 0.02	1.26 ± 0.01	–	<0.8	0.78 ± 0.03	<0.02	0.83 ± 0.03	$0.582^{+0.006}_{-0.002}$	D
58362	1.76 ± 0.03	1.24 ± 0.01	–	<0.7	0.77 ± 0.02	<0.09	0.82 ± 0.03	$0.579^{+0.010}_{-0.005}$	D
58363	1.80 ± 0.02	1.19 ± 0.02	–	<2	0.74 ± 0.02	<0.08	0.82 ± 0.02	0.54 ± 0.01	D
58364	1.79 ± 0.02	1.17 ± 0.01	–	<1	0.73 ± 0.03	<0.1	0.79 ± 0.04	$0.549^{+0.010}_{-0.007}$	D
58368	1.76 ± 0.03	1.04 ± 0.02	–	<4	0.68 ± 0.03	<0.07	0.72 ± 0.04	$0.500^{+0.020}_{-0.004}$	D
58373	1.83 ± 0.03	0.841 ± 0.009	–	<0.4	0.49 ± 0.03	<0.06	0.53 ± 0.04	$0.363^{+0.008}_{-0.003}$	D
58374	1.86 ± 0.04	0.78 ± 0.01	–	<0.3	0.46 ± 0.02	<0.08	0.50 ± 0.03	$0.345^{+0.007}_{-0.010}$	D

This paper has been typeset from a \LaTeX file prepared by the author.